Neuroscience

Inference technique for the synaptic conductances in rhythmically active networks and application to respiratory central pattern generation circuits

Reviewed Preprint
v1 • October 25, 2024
Not revised

Yaroslav I Molkov ✉, **Anke Borgmann, Hidehiko Koizumi, Noriyuki Hama, Ruli Zhang, Jeffrey C Smith**

Department of Mathematics and Statistics, Neuroscience Institute, Georgia State University, Atlanta, GA, United States • Cellular and Systems Neurobiology Section, NINDS, NIH, Bethesda, MD, United States • Department of Neural and Muscular Physiology, Shimane University School of Medicine, Izumo City, Japan

Abstract

Unraveling synaptic interactions between excitatory and inhibitory interneurons within rhythmic neural circuits, such as central pattern generation (CPG) circuits for rhythmic motor behaviors, is critical for deciphering circuit interactions and functional architecture, which is a major problem for understanding how neural circuits operate. Here we present a general method for extracting and separating patterns of inhibitory and excitatory synaptic conductances at high temporal resolution from single neuronal intracellular recordings in rhythmically active networks. These post-synaptic conductances reflect the combined synaptic inputs from the key interacting neuronal populations and can reveal the functional connectome of the active circuits. To illustrate the applicability of our analytic technique, we employ our method to infer the synaptic conductance profiles in identified rhythmically active interneurons within key microcircuits of the mammalian (mature rat) brainstem respiratory CPG and provide a perspective on how our approach can resolve the functional interactions and circuit organization of these interneuron populations. We demonstrate the versatility of our approach, which can be applied to any other rhythmic circuits where conditions allow for neuronal intracellular recordings.

eLife Assessment

The paper describes a novel approach for inferring features of synaptic networks from recordings of individual cells within the network. The paper will be a **valuable** contribution to those studying central pattern generators, including those involved in respiration. However, the theoretical approach to drawing inferences regarding the underlying synaptic currents is **incomplete** as it relies on unsupported simplifying assumptions.

https://doi.org/10.7554/eLife.101959.1.sa2

Introduction

Rhythmic neural circuits, which are ubiquitous in nervous systems (Buzsáki, 2006), generate spatiotemporal patterns of activity by synaptic interactions between neuronal populations, and unraveling the synaptic inputs to circuit neurons at high temporal resolution in the active networks is a major experimental problem in neurobiology for understanding circuit functional dynamics and architecture. Solving this problem ultimately requires electrophysiological methods to extract dynamic patterns of synaptic conductances in post-synaptic neurons from intracellular recordings during network activity. These patterns often involve temporally complex excitatory and inhibitory synaptic inputs, and thus methods to extract these inputs must be able to delineate the excitatory and inhibitory components, which can be superimposed during circuit activity, complicating the problem. In this study we have developed a robust and versatile technique for extracting and separating patterns of inhibitory and excitatory synaptic conductances from intracellular recording data that is applicable to any periodically active network. We designed our method to be compatible with various experimental setups, including current-clamp and voltage-clamp protocols, by focusing on the fundamental principles of electrophysiology and network dynamics. Our technique ensures high-resolution temporal profiling of synaptic inputs, making it adaptable to a wide range of rhythmically active neuronal circuits such as vertebrate and invertebrate motor pattern generation (CPG) networks (e.g., (Calabrese & Marder, 2024)), and cortical circuit rhythms (Yuste *et al*., 2005). This generalizability highlights the potential of our approach to provide new insights into the functional organization and dynamics of diverse rhythmic neural circuits. Our approach extends previously proposed methods for extracting dynamic patterns of input synaptic conductances from intracellular recordings from neurons in a variety of circuits (Borg-Graham *et al*., 1998; Anderson *et al*., 2000; Shu *et al*., 2003; Berg *et al*., 2007; Endo & Kiehn, 2008; Wright & Calabrese, 2011) by providing nearly continuous, high-resolution readouts of excitatory and inhibitory synaptic conductances that are essential for deciphering circuit functional interactions.

To illustrate the utility of our technique, we applied this to circuits in the mammalian brainstem respiratory CPG, which is the fundamental rhythmic neural system that generates and controls breathing movements that are critical for homeostatic regulation of oxygen, carbon dioxide and pH in the brain and body (Feldman & Smith, 1995; Richter & Smith, 2014). These circuits are continuously active in various experimental preparations and the experimental accessibility of these circuits provides the opportunity to apply our methods to investigate cellular and network electrophysiological processes underlying rhythmic motor pattern generation in a physiologically important mammalian system (Richter & Spyer, 2001; Smith *et al*., 2013). The rhythmic patterns of alternating inspiratory and expiratory phase neuronal activities that coordinate activity of spinal and cranial motoneurons during breathing originate within interacting pontine-medullary excitatory and inhibitory circuits in the brainstem (Cohen, 1979; Bianchi *et al*., 1995; Feldman & Smith, 1995; Richter, 1996; Smith *et al*., 2013). We have targeted specific respiratory microcircuits in the medulla of mature rat brainstem-spinal cord preparations *in situ* containing a variety of neuronal phenotypes and synaptic interactions that are key to the operation of the respiratory CPG. This allowed us to perform single neuron intracellular recordings from various neuronal types in different microcircuits, test different recording protocols to assess the robustness of our approach, and provides examples of how our technique can extract complex patterns of synaptic conductances at high temporal resolution in different types of rhythmic neurons. We illustrate how the synaptic conductance profiles throughout the respiratory cycle imply a “functional connectome” of respiratory circuit interactions, demonstrating the efficacy of our technique to provide novel information on circuit dynamic organization and operation.

Results

The general theoretical aspects of our approach for analyzing neuronal excitatory and inhibitory conductances from intracellular recordings in rhythmic circuits, and their specific application to the rhythmically active respiratory circuits, are delineated below. Our objective was to extract synaptic conductance profiles representing nearly continuous readouts of excitatory and inhibitory synaptic inputs from the neuronal recordings throughout a cycle of periodic neural activity— the respiratory cycle in our illustration. Any periodic activity can be analyzed in the same way that we describe in this illustration below.

Reconstruction of synaptic inputs from intracellular recordings

The reconstruction of synaptic conductance profiles is based on the current balance equation:

$$g_{leak}(E_{leak} - V_m(t)) + g_i(t)\big(E_i - V_m(t)\big) + g_e(t)\big(E_e - V_m(t)\big) + I_{inj}(t) = 0 \qquad (1)$$

where g_{leak} and E_{leak} are the conductance and the reversal potential of the leak current respectively, $g_i(t)$ and $g_e(t)$ are inhibitory and excitatory conductances (subject to retrieval), E_i and E_e are reversal potentials of inhibitory and excitatory synaptic currents, and $I_{inj}(t)$ is the injected current. Equation (1) implies that the membrane potential of the cell after short-time-scale fluctuations are filtered out is in instantaneous equilibrium, i.e., the membrane time constant C/g_{leak} (where C is membrane capacitance) is much shorter than the time scale of the synaptic conductance variations.

The phase of the respiratory cycle was defined as a piece-wise linear function of time in the following way: $\phi(t) = (t - t_k)/(t_{k+1} - t_k)$, for times t between the time moments of two consecutive inspiratory phase onsets t_k and t_{k+1}. Our approach was based on the idea that in a network exhibiting periodic dynamics, the synaptic conductances depend on the cycle phase and not on time explicitly, so that $g_{i,e}(t) = g_{i,e}(\phi(t))$. The respiratory cycle was divided into 100 bins of phase values, and for each bin the time moments $\{t_{ik}: \phi(t_{ki}) \in [\phi_i, \phi_{i+1}]\}$ that correspond to phases in the bin were collected. For each phase bin i of the respiratory cycle, the relationship between the injected current $I_{inj}(t_{ik})$ and the membrane potential $V_m(t_{ik})$, where t_k are the times that correspond to the phase bin, appears fairly linear (see **Figure 1B** and **Supplemental Figure 3**). Therefore, by linear regression we can find the slope and V-intercept of this dependence in the form:

$$V_m(t_k) = V_0(\varphi) + R(\varphi) \cdot I_{inj}(t_k) + \delta V_m(t_k) \qquad (2)$$

where $\phi = (\phi_i + \phi_{i+1})/2$ is the center of the bin. The slope $R(\phi)$ represents the total resistance, the intercept $V_0(\phi)$ is the effective resting potential for the phase of the cycle ϕ, and $\delta V_m(t_k)$ are random fluctuations of the membrane voltage. Total conductance $G(\phi)$ was calculated as the reciprocal of the total resistance, $G(\phi) = 1/R(\phi)$. The total conductance has static (phase-independent) and dynamic (phase-dependent) components. The latter is assumed to be a sum of dynamic components of the inhibitory and excitatory synaptic conductances. Synaptic conductances can also have static components whose combination cannot be distinguished from a static conductance of any other nature. Accordingly, we can think of the total conductance as a superposition of inhibitory and excitatory conductances whose static components form a static component of the total conductance, and their dynamic components underlie dynamic changes in the total conductance. Hence, the total current can be thought as a combination of the inhibitory and excitatory currents:

$$G(\varphi)(V_m - V_0(\varphi)) = G_i(\varphi)(V_m - E_i) + G_e(\varphi)(V_m - E_e), \qquad (3)$$

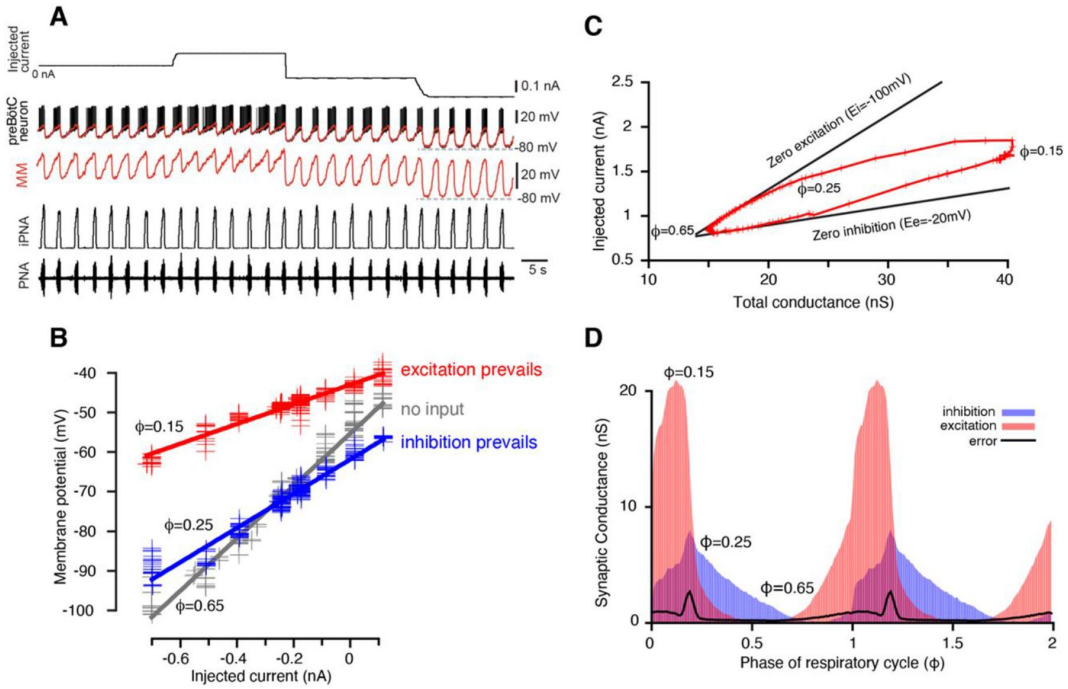

Figure 1.

Reconstruction of synaptic conductance profiles.

(**A**) An example of the intracellular recording from a rhythmic inspiratory neuron (2nd trace from top) during the stepwise current injection (top trace) protocol that we used for our analyses. Extracellular recording of phrenic nerve activity (PNA, bottom trace) and integrated PNA (iPNA, 4rd trace from top) are used for reference. The red trace shows a moving median (MM) filtration of the voltage at higher voltage resolution in the 3rd trace. The MM filters out the spikes while preserving slow voltage waves. (**B**) Plots of injected current vs. membrane potential of a preBötC inspiratory neuron corresponding to three selected values of the respiratory cycle phase (φ). Straight lines of the same colors show best linear fits. The parameters of the fits – the slope and *y*-intercept – are used to estimate the total resistance and the resting potential, respectively, for each phase of the cycle. (**C**) A typical example of the wedge diagram. Red plusses represent parameters of linear regressions for 100 phase values. The x-coordinate of each point is the total conductance $G(\varphi) = 1/R(\varphi)$, and the y-coordinate is $I_0(\varphi)$ (see Eqs. (2) and (11)). Thick black lines are zero excitation (upper boundary) and zero inhibition (lower boundary) lines, respectively (see Eqs. (13) and (14)). The slopes of the lines correspond to the reversal potentials for inhibition and excitation. (**D**) Calculated dynamic components of synaptic conductances from the same recording using Eqs. (6-9) as functions of the phase of the respiratory cycle. Two cycles are shown with integer values of the phase (0, 1, 2) corresponding to a transition from expiration to inspiration. The excitatory synaptic conductance is shown in red, and the inhibitory conductance is shown in blue.

where $G_i(\phi)$ and $G_e(\phi)$ are inhibitory and excitatory synaptic conductances, and E_i and E_e are corresponding reversal potentials. This equation must be fulfilled for any V_m, therefore

$$G(\varphi) = G_i(\varphi) + G_e(\varphi), \tag{4}$$

$$G(\varphi)V_0(\varphi) = G_i(\varphi)E_i + G_e(\varphi)E_e. \tag{5}$$

Solving this system of equations for the synaptic conductances yields

$$G_i(\varphi) = G(\varphi)(E_e - V_0(\varphi))/(E_e - E_i), \tag{6}$$

$$G_e(\varphi) = G(\varphi)(V_0(\varphi) - E_i)/(E_e - E_i). \tag{7}$$

To find the dynamic components of the synaptic conductances $\Delta G_i(\phi)$ and $\Delta G_e(\phi)$ we subtract their minimal values over the respiratory cycle:

$$\Delta G_i(\varphi) = G_i(\varphi) - \min_\varphi G_i(\varphi), \tag{8}$$

$$\Delta G_e(\varphi) = G_e(\varphi) - \min_\varphi G_e(\varphi). \tag{9}$$

Finally, we can use the sum of the minimal values found as an estimate for the leak conductance:

$$g_{leak} = \min_\varphi G_i(\varphi) + \min_\varphi G_e(\varphi). \tag{10}$$

Reversal potential estimation

It is possible that during a certain part of the cycle, a neuron receives only one type of synaptic input, inhibitory or excitatory. Below is how this fact can be exploited for obtaining the estimates of reversal potentials for inhibition or excitation. For inhibition, after introducing

$$I_0(\varphi) = -G(\varphi)V_0(\varphi) \tag{11}$$

in (5) and combining (4) and (5) we get:

$$I_0(\varphi) = -E_iG(\varphi) - G_e(\varphi)(E_e - E_i). \tag{12}$$

Since the total excitatory synaptic conductance $G_e(\phi)$ is greater or equal to its static component $G_e^0 = \min_\varphi G_e(\varphi)$,from (12) it follows that a straight line on the (G, I)-plane described by

$$I_0(\varphi) = -E_iG(\varphi) - G_e^0(E_e - E_i) \tag{13}$$

serves as an upper boundary of the reconstructed trajectory $\{(G(\phi), I_0(\phi)), \phi \in [0,1]\}$. If we suppose that the neuron receives only phase-dependent inhibition in a certain range of phase, i.e., the excitatory synaptic conductance is equal to its static component in this range, $G_e(\varphi) = G_e^0$, then the trajectory moves strictly along the line described by (13) which can be referred to as a *zero excitation line*. By identifying the upper portion of the trajectory with nearly linear behavior we can perform linear regression of this portion to find its slope $-E_i$, and thus estimate the reversal potential for inhibition (see **Figure 1C**). Similarly, for the phases of the cycle where only excitatory input is present, we can derive:

$$I_0(\varphi) = -E_eG(\varphi) + G_i^0(E_e - E_i) \tag{14}$$

where $G_i^0 = \min_\varphi G_i(\varphi)$ is a static component of the inhibitory conductance and call it the *zero inhibition line*. The latter obviously serves as a lower boundary of the trajectory. Together the zero excitation and zero inhibition lines form a wedge that bounds the trajectory, so hereinafter we refer to such plots as *wedge diagrams* (**Figure 1C**).

Interestingly, the linear upper boundary of the trajectory was seen in almost all recordings processed implying that, first, during certain phase(s) of the respiratory cycle the interneurons indeed receive only inhibitory input, and second, we could use the identified parameters of the zero-excitation line to measure the inhibitory reversal potential. The same approach might be applied for the determination of the reversal potential for excitation if there was a certain range of phases when a cell received the excitatory input only. Since E_e is expected to be close to 0 mV, this would be clearly identifiable by the presence of a nearly horizontal part of the curve serving as a lower boundary of the same. This kind of behavior was not found in most of the recordings, so, as commonly accepted, E_e was set to -10 mV in those cases. However, as we demonstrate below, variation of reversal potentials over a wide range of possible values does not affect the shape of synaptic conductance profiles qualitatively.

Firing patterns, synaptic input conductances, and inferred functional connectome of respiratory interneurons: an illustration

For our illustration of extracting synaptic conductances with the above approach, we targeted neurons in key interacting respiratory circuits located in discrete bilateral regions of the ventrolateral medulla, specifically in the preBötzinger complex (preBötC) region, which contains local excitatory and inhibitory circuit neurons critical for generating rhythmic inspiratory activity, and the adjacent more rostral Bötzinger complex (BötC) region (refer to **Supplemental Figure 1**), containing neurons generating rhythmic expiratory activity that interact with preBötC circuits, including by inhibitory circuit connections (e.g., (Lindsey *et al*., 2012; Smith *et al*., 2013; Molkov *et al*., 2017; Ausborn *et al*., 2018). Thus, targeting these regional microcircuits allowed us to test our methods for extracting various patterns of excitatory and inhibitory synaptic inputs in two functionally distinct microcircuits. Also, there are various electrophysiological phenotypes of respiratory neurons with different patterns of neuronal spiking activity during the respiratory cycle in these regions, thus providing a diversity of rhythmic neuronal types to correlate with synaptic input patterns from our analysis, which is useful for illustrating the utility of our techniques for delineating various functional synaptic interactions. We have used sharp microelectrode intracellular recordings in mature rat brainstem-spinal cord preparations *in situ* (see Materials and methods) for our analysis since this approach allowed us to readily record deep in the brainstem in these targeted regions from multiple neurons under current- and voltage-clamp with a single electrode. This provides complementary information to test the robustness of our approach, which should be insensitive to the mode of intracellular recording. Although our techniques can be applied to any type of rhythmic neuron, we specifically targeted and analyzed interneurons, verified by immunochemistry (as described below and in Material and methods), which are the most technically challenging to record from due to small neuronal sizes and potential recording instability, but are functionally critical for analyzing synaptic mechanisms of neural activity pattern generation. Thus, we could test how our technique performs for important neuronal populations under recording conditions that would likely be encountered for many rhythmic interneuronal circuits in nervous systems.

Firing patterns of respiratory interneurons

Under normal physiological conditions the neuronal activity during the respiratory cycle consists of three main activity phases [inspiratory (I), post-inspiratory (post-I), and stage 2 or late expiratory (E2)] that are well documented in the literature (e.g., (Lindsey *et al*., 2012; Richter & Smith, 2014). Previously described respiratory populations based on their specific firing patterns in relation to these different phases of the cycle (see **Figure 2**) include pre-inspiratory/inspiratory (pre-I/I), ramping inspiratory (ramp-I), early-inspiratory (early-I), late

inspiratory (late-I), post-inspiratory (post-I) and augmenting expiratory (aug-E, active during E2) neurons. We have recorded neurons from all these populations (**Figure 2**) and have analyzed and presented representative synaptic input patterns (**Figure 3**) for each electrophysiological phenotype. In some cases, as an informative addition to our electrophysiological analyses, we labeled the recorded neurons by intracellular injection of biocytin contained in the electrode recording solution (see Materials and methods) for subsequent histological verification (**Supplemental Figure 1**) of the recording location, interneuron identification, and in some cases neurotransmitter phenotype by immunohistochemistry (n=34 neurons total labeled). The latter enabled us to identify inhibitory neurons (glycinergic or GABAergic) (**Supplemental Figure 2**) for five of the neuron types (pre-I/I, ramp-I, early-I, post-I, aug-E) as described below, which aids in circuit analysis and the corroboration of inhibitory inputs from neurons with particular firing patterns.

Synaptic conductances and functional connectome of respiratory interneurons

Figure 3 shows the synaptic conductance profiles of the major interneuronal electrophysiological phenotypes whose firing patterns are illustrated in **Figure 2**. Within one population of the same electrophysiological phenotype, patterns of synaptic inputs were qualitatively similar, although there was neuron-to-neuron variability in calculated conductance values and details of the conductance profiles could vary (**Figure 3**) among multiple examples of each type of recorded neurons. From these temporal patterns of synaptic conductances, as explained below we infer functional connectomes or circuit motifs for each electrophysiological phenotype as illustrated in **Figure 4**, which is an important outcome of our analyses. In general, these circuit connections motifs are constructed by considering that the different components of the synaptic conductance profiles are formed by convergent inputs from neuronal populations of specific phenotypes and, therefore, can be interpreted as reflecting activity patterns of these pre-synaptic populations. By matching activity patterns with patterns of synaptic inputs in the recorded post-synaptic neurons, we can suggest functional connections between neuronal populations. The information on inhibitory transmitter phenotype for neurons with different firing patterns was also considered and indeed corroborates that subsets of the presynaptic neurons are inhibitory as inferred from the conductance profiles, which gives additional confidence in the correlation between pre-synaptic firing patterns and likely post-synaptic interactions.

To illustrate in more detail how we have reconstructed the circuit connection motifs in **Figure 4**, we describe how we interpret and translate the synaptic conductance profiles for each lectrophysiological phenotype. Pre-I/I cells (n=25 neurons recorded in the preBötC) in all cases received decrementing expiratory inhibition, and augmenting excitation during late expiration as well as strong ramping inspiratory excitation (**Figure 3A1-5**). As shown In **Figure 4A1**, a straight-forward interpretation of this pattern of inputs is that the pre-I/I population receives inhibitory inputs from post-I spiking neurons and excitatory inputs from aug-E and ramp-I populations. Alternatively, since a combination of aug-E and ramp-I excitatory inputs is qualitatively similar to an input from the pre-I/I population itself, it is also possible that excitatory pre-I/I neurons are recurrently interconnected within this population (**Figure 4A2**). These possibilities are not mutually exclusive, and both connectivity patterns could be expressed in the respiratory circuits. We labeled 13 of these pre-I/I neurons during recording, two of which were identified as inhibitory neurons by neurotransmitter immuno-labeling for glycine or GABA (1 glycinergic and 1 GABAergic neuron identified), which is incorporated in **Figure 4F1**.

Neurons with the ramp-I spiking patterns (n=24 recorded in preBötC) also received ramping inspiratory phase excitation, but unlike some pre-I/I cells, they generally showed strong synaptic inhibition throughout the post-inspiratory and late-expiratory (E2) phases (**Figure 3B1-5**). Some

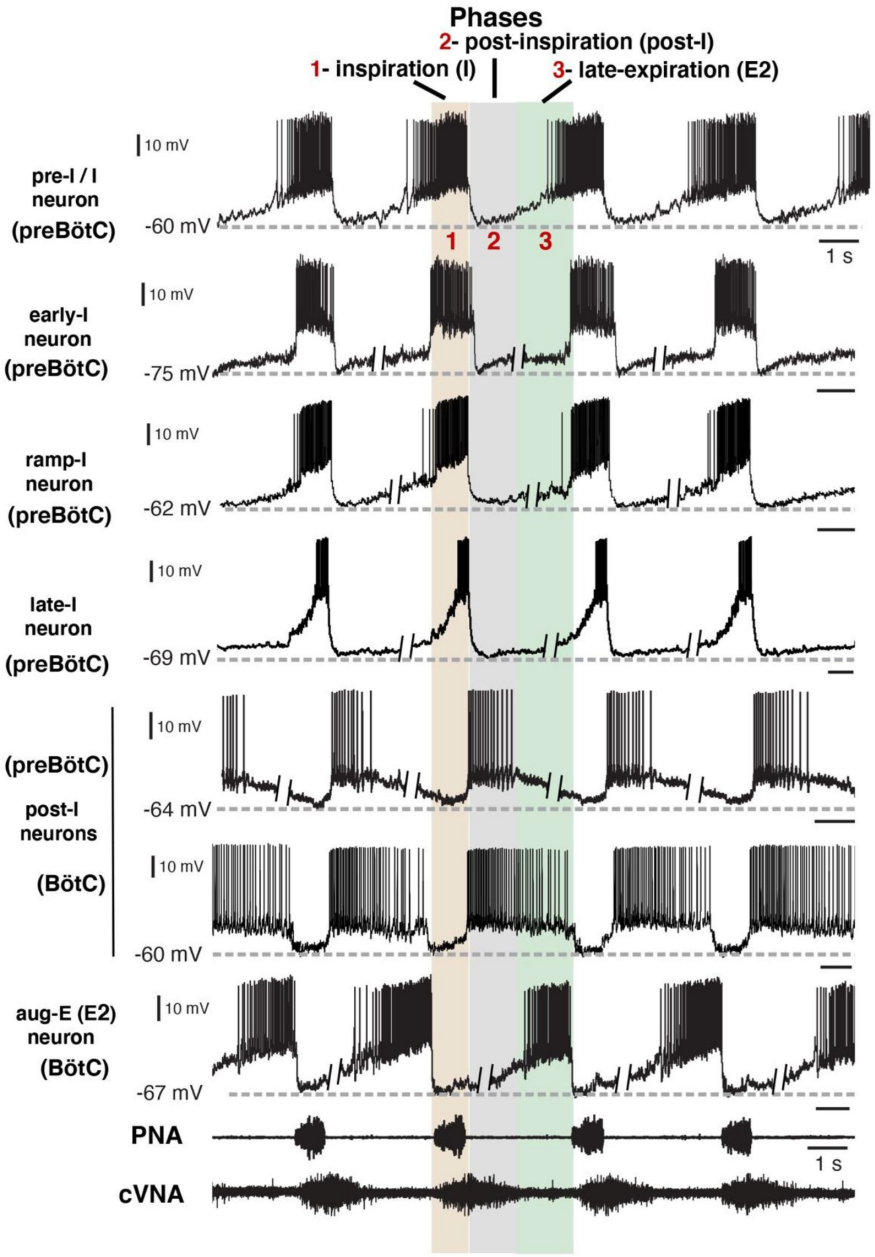

Figure 2.

Firing patterns of respiratory interneurons.

The traces are current clamp intracellular recordings from different types of respiratory neurons distinguished by their action potential firing patterns and activity during different respiratory cycle phases [inspiratory (I), post-I, or late-expiratory/E2 phase]. Extracellular recordings of the phrenic nerve activity (PNA) and central vagus nerve activity (cVNA) are shown below as reference. The nerve recordings were obtained simultaneously with the pre-I/I neuron recording. All other neuron recordings were obtained from different experimental preparations and were composited and aligned according to phases of the cycle as indicated at the top. This was done by deleting segments (as indicated) of the membrane potentials during the expiratory phases, since the expiratory intervals largely determine the discharge frequencies which are variable between the *in situ* preparations, while the inspiratory phase durations are very similar. All neurons included in our study exhibited rhythmic firing patterns consistent with the three-phase organization of the cycle and can be arranged in this format for purposes of illustration. Regions of the ventrolateral medulla (preBötC or BötC) where these example recordings were obtained, as verified histologically, are indicated.

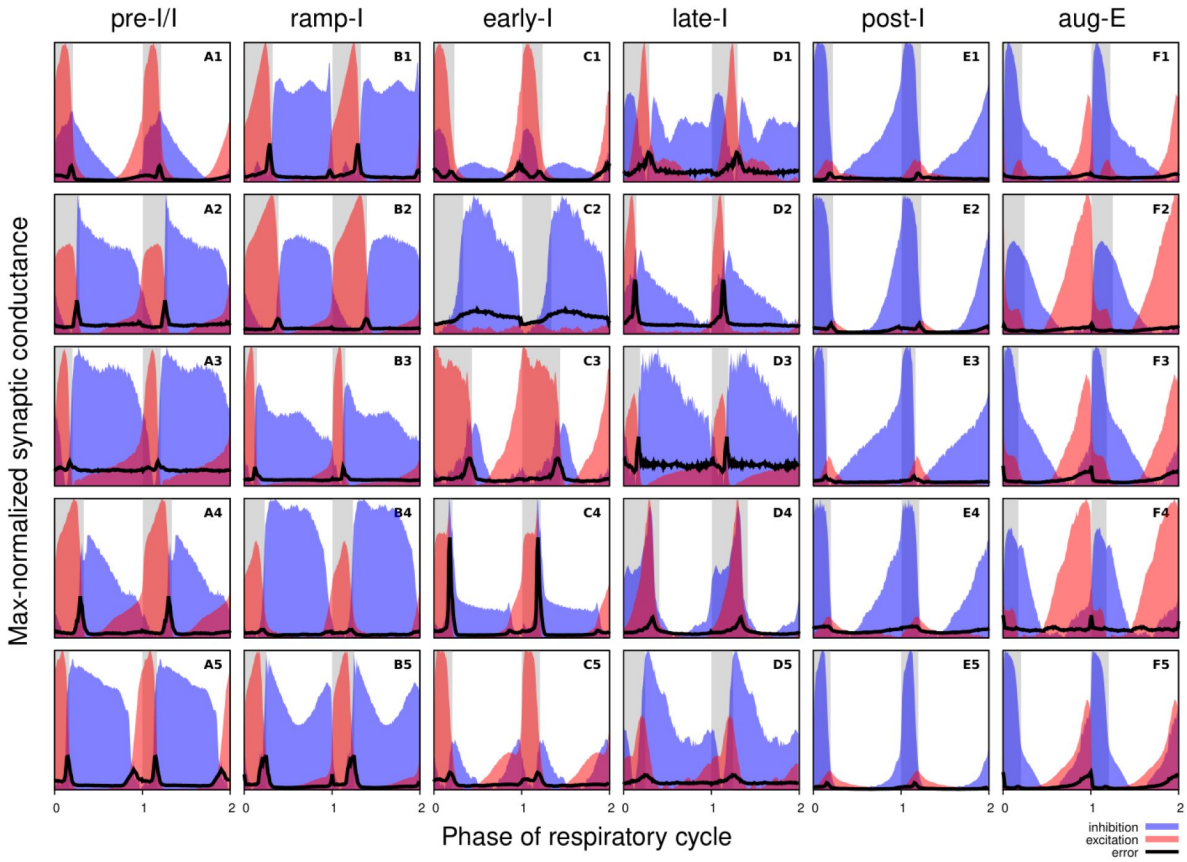

Figure 3.

Synaptic conductance profiles of major respiratory neuronal phenotypes.

Each panel depicts how the dynamic components of excitatory (red) and inhibitory (blue) synaptic conductances, normalized to the maximal value, vary with the cycle phase for an individual neuron. Neuronal firing phenotypes are listed on the top. Two respiratory cycles are shown so that transitions between the respiratory phases are clearly seen. The inspiratory phases are highlighted by grey bars. Integer phase values (0, 1, 2) correspond to transitions from expiration to inspiration as determined by onset of the phrenic motor output recorded simultaneously. The error for each phase value is indicated by a thick black line in each panel.

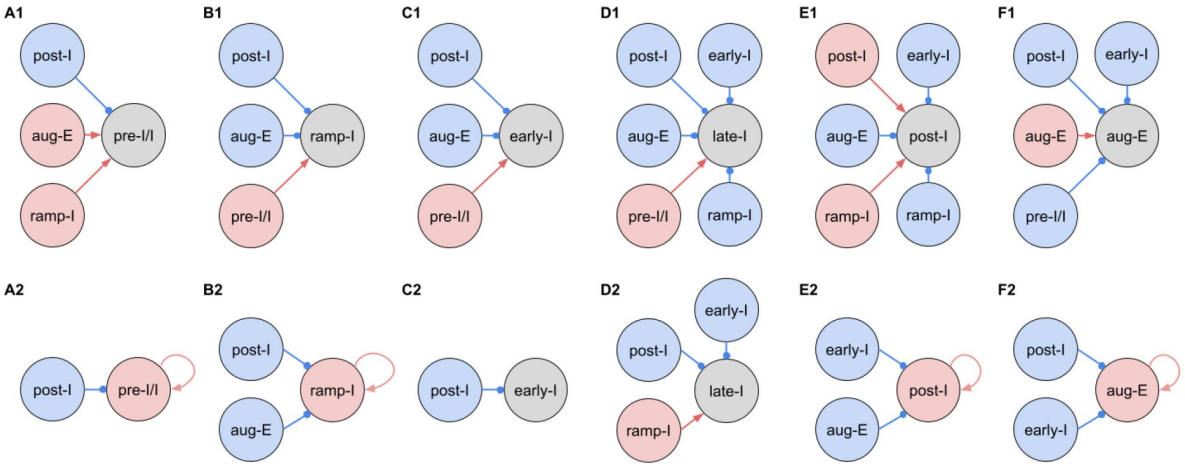

Figure 4.

Inferred connections between different respiratory interneuronal populations.

By matching the firing phenotype of the receiver neuron and its synaptic inputs we infer possible motifs of interactions between the functional populations of the active network. In this representation, we assume that the functional connection between populations is present, if a post-synaptic neuron of a particular firing phenotype has a dynamic component of the synaptic conductance statistically significantly different from zero (see Materials and methods: Statistical significance) in the phase range corresponding to the activity pattern of the pre-synaptic population. Here we show two examples of such inferences for each phenotype representing the most straightforward interpretation of synaptic inputs (***A1, B1, C1, D1, E1 and F1***) as well as interactions involving the least number of populations (***A2, B2, C2, D2, E2 and F2***), reflecting the cell-to-cell variability in conductance profiles with some neurons within a given electrophysiological phenotype exhibiting the smaller set of synaptic inputs. Possible inhibitory/excitatory connections are shown by blue/red lines ending with blue circles/red arrows originating from presynaptic neurons and terminating at the post-synaptic neurons. Inhibitory sources are shown in blue, and the excitatory sources are shown in red. These circuit motifs are consistent with the patterns of synaptic inputs to the various neurons, as described in the text for each electrophysiological phenotype, and account for our immuno-histochemical identification of inhibitory neurons as subpopulations of most of the electrophysiological types as indicated in the text.

of these neurons also received excitatory input during the E2 expiratory/pre-inspiratory phase. Therefore, it is reasonable to suggest that ramp-I neurons receive inhibitory inputs from post-I and aug-E populations as well as an excitatory input from pre-I/I neurons (**Figure 4B1**). Another possibility is that the excitatory ramp-I neurons not receiving excitation during the pre-inspiratory phase have recurrent excitation within their population (**Figure 4B2**). Four out of 7 of these neurons were labeled in the preBötC and identified as inhibitory (glycinergic) neurons (incorporated in **Figures 4D1&4E1**).

All early-I spiking neurons (n=6 in preBötC) showed decrementing expiratory phase inhibition (**Figure 3C1-5**). Most of these cells also received pre-inspiratory/late expiratory and inspiratory excitation (**Figure 3C1, 3-5**), while some of them did not (**Figure 3C2**), which we interpret as shown in **Figures 4C1 and 4C2**, respectively. The excitatory pre-I/I input can also be a combination of aug-E and ramp-I excitation as in **Figure 4A1**. One of the three labeled early-I neurons was identified as an inhibitory (GABAergic) neuron (**Supplemental Figure 2**), corroborating the early-I inhibitory inputs inferred from conductance profiles shown in **Figures 4 D1&2, 4E1&E2, 4F1&F2**.

Synaptic inputs to late-I cells (n=6 in preBötC) were similar to ramp-I neurons (**Figure 3D1-5**) plus concurrent, inspiratory phase inhibition. So, in addition to inhibitory inputs from post-I and aug-E neurons and pre-I/I (in some cases) and ramp-I excitation, they likely receive inhibitory inputs from early-I spiking neurons (**Figure 4D1**). Some of these cells showed neither inhibition nor excitation at the end of expiration (**Figure 3D2**), so they might receive no aug-E inhibition and ramp-I rather than pre-I/I excitation (**Figure 4D2**). These neurons were infrequently recorded, and none were successfully labeled for neurotransmitter type identification.

Post-I spiking neurons (n=40: 25 in preBötC, 15 in BötC), that always exhibit a decrementing firing pattern during expiration, received strong decrementing inhibition during inspiration, and incrementing inhibition during late expiration (**Figure 3E1-5**). They also showed a relatively weak excitation during post-inspiration, usually accompanied by comparable in magnitude ramping excitation during inspiration. The corresponding circuit elements representing inputs to the post-I neurons are shown in **Figure 4E1**. Since post-I neurons receive post-I excitation, it is possible that excitatory post-I cells form a population with recurrent excitatory interconnections. Besides, some of these neurons did not have any significant excitatory input during inspiration (**Figure 3E3**). The latter possibilities are shown in **Figure 4E2**. Eight of the 20 post-I neurons labeled (5 in preBötC and 3 BötC neurons) were identified as glycinergic (**Supplemental Figure 2**), consistent with a previous study (Ezure *et al*., 2003), and corroborating the post-I inhibitory inputs shown in **Figures 4A1&2, 4B1&2, 4C1&2, 4D1&2, 4F1&2**.

Finally, all the aug-E spiking neurons (n=19 recorded: 9 neurons in preBötC, 10 in BötC) received decrementing inhibitory inputs during expiratory and inspiratory phases as well as an excitatory input that started in the middle of expiration and incremented towards the end of expiration (**Figure 3F1-5**).

Some of these neurons received pre-inspiratory inhibition. We interpret this as the aug-E population receiving inputs from early-I, post-I and pre-I/I inhibitory populations and the excitatory input from aug-E neurons (**Figure 4F1**). Similar to other interpretations, it is also possible that the excitatory aug-E neurons form a population with recurrent excitation with an augmenting pattern that matches their activity profile, while some of these neurons do not receive pre-I inhibition (**Figure 4F2**). Three out of 6 of these neurons labeled were identified as glycinergic neurons (1 preBötC neuron and 2 BötC neurons) (**Supplemental Figure 2**), as inferred from the synaptic conductance profiles in **Figures 4B1&2, 4C1, 4D1, 4E1**.

Validating reliability of inferred synaptic conductance profiles

Synaptic conductance profiles from current- and voltage-clamp recordings

The traditional way to measure transmembrane currents is by voltage-clamp intracellular recordings. Using this experimental protocol, the membrane potential of the neuron is held at a constant level thus maintaining all voltage-dependent membrane currents at their steady states. Therefore, in voltage-clamp conditions any total current variations result exclusively from time-varying synaptic inputs, while in the current-clamp protocol variations of the voltage can potentially be contaminated by transient dynamics of the voltage-gated channels. However, the implementation of the voltage-clamp protocol is technically far more challenging with sharp high-impedance microelectrodes than injecting a constant current. By design, our technique is indifferent to what strategy is used for the injected current variations, so we performed both current- and voltage-clamp recordings from select neurons (n=10) where the voltage-clamp could be satisfactorily established following the current-clamp recording in each of these neurons and compared the results of the synaptic input interferences as a test of the reliability of our methods.

Figure 5 shows the excitatory and inhibitory synaptic conductance profiles extracted from current-(left) and voltage-clamp (right) segments of the intracellular recordings for 3 different types of representative neurons. It is evident that the shapes of the conductance profiles as well as the relationship between the excitatory and inhibitory conductances extracted are very similar. Quantitative variations in the amplitude of the synaptic inputs are similar to those observed when using different epochs of the same current-clamp recordings (see below). Thus, we conclude that our synaptic conductance inferences obtained by current clamp recordings favorably match the conductance profiles obtained from direct recordings of synaptic currents during voltage clamp.

Uncertainties concerned with estimates of synaptic reversal potentials

As noted, it was not always possible to identify linear portions of GI-contours suitable for reliable estimation of the reversal potentials. In addition, the procedure described does not imply an unequivocal way for finding the errors for the reversal potential estimates. Accordingly, for the synaptic input classification purposes, we varied the reversal potentials in the predefined ranges when using **Eqs. (6)** and **(7)** to calculate the synaptic conductances. We used the following ranges: [-20, 0] mV and [-110, -90] mV for the reversal potentials for excitation and inhibition, respectively. **Figure 6** illustrates that although the absolute values of the conductances vary to some extent as we vary the reversal potentials, the shape of their reconstructed profiles remains consistent.

Evaluating the effects of non-stationarity of the intracellular recordings

Our approach implicitly assumes that the intrinsic properties of the recorded neurons do not change (much) throughout the epoch used for the calculations. To verify the plausibility of this hypothesis, whenever possible we used two different epochs from the same recordings satisfying the criteria formulated in the *Preprocessing* section of the Methods for the complete analysis. We found that differences between the results for different epochs in most cases were comparable to those observed in the recordings obtained by current- and voltage-clamp protocols from the same neuron. **Figure 7** shows the results for two adjacent non-overlapping epochs for three different neurons.

In summary, our evaluation of the major assumptions and potential sources of error with our procedures for extracting temporal patterns of synaptic conductances, including recording procedures, and cycle phase-dependent linearity of current-voltage relations (**Supplemental**

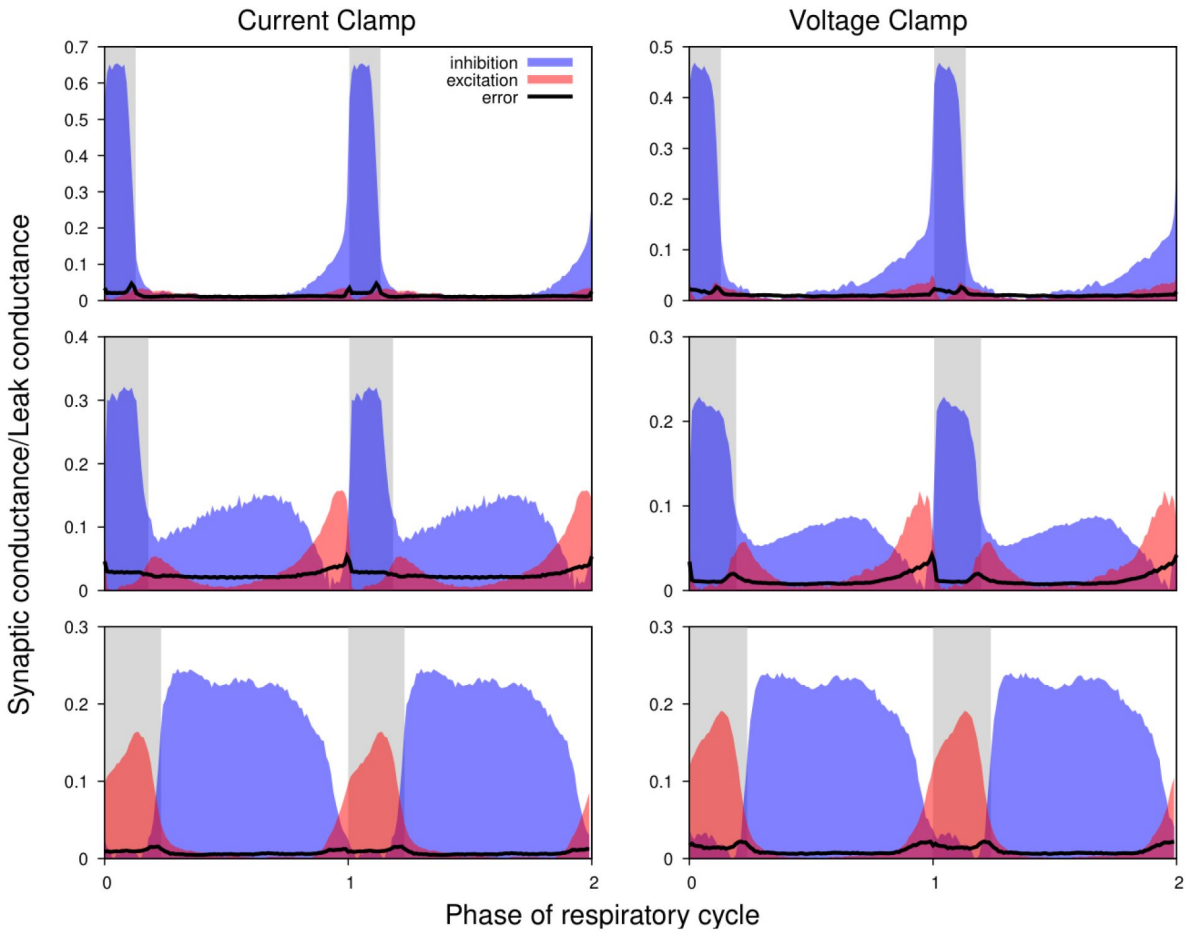

Figure 5.

Comparison of the synaptic conductance profiles reconstructed from current- and voltage-clamp recordings.

Conductance profiles for three representative preBötC neurons are illustrated (from current-clamp recordings at left and voltage-clamp recordings from the same neurons at right). Two respiratory cycles are shown for each neuron (post-I, top; aug-E, middle; ramp-I, bottom panels) with inspiratory phases highlighted by gray bars. Calculated synaptic conductances are normalized by the estimates of the leak conductance. While the absolute conductance values may vary, the shapes of the synaptic conductance profiles as well as the relationship between the excitatory and inhibitory conductances are consistent across these recording protocols.

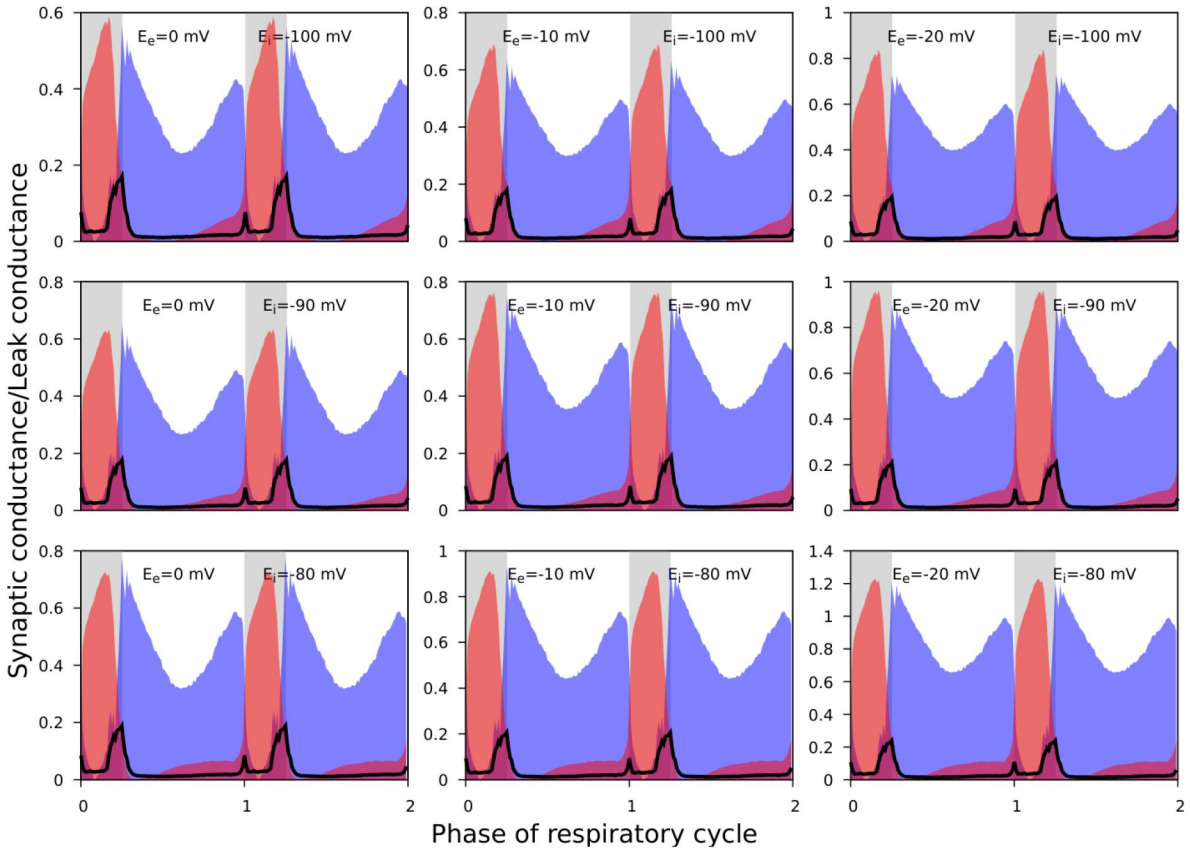

Figure 6.

The effect of reversal potential variation on the synaptic input reconstruction results.

We used the recording of the ramp-I neuron shown in **Fig. 3B5** and recalculated its synaptic conductances for different combinations of the inhibitory and excitatory reversal potential values as indicated in each plot. Synaptic conductances are normalized by the estimates of the leak conductance. While the absolute conductance values vary with the reversal potentials, the shapes of the synaptic profiles as well as the relationship between the excitatory and inhibitory conductances are consistent across different values of the excitatory and inhibitory reversal potentials used.

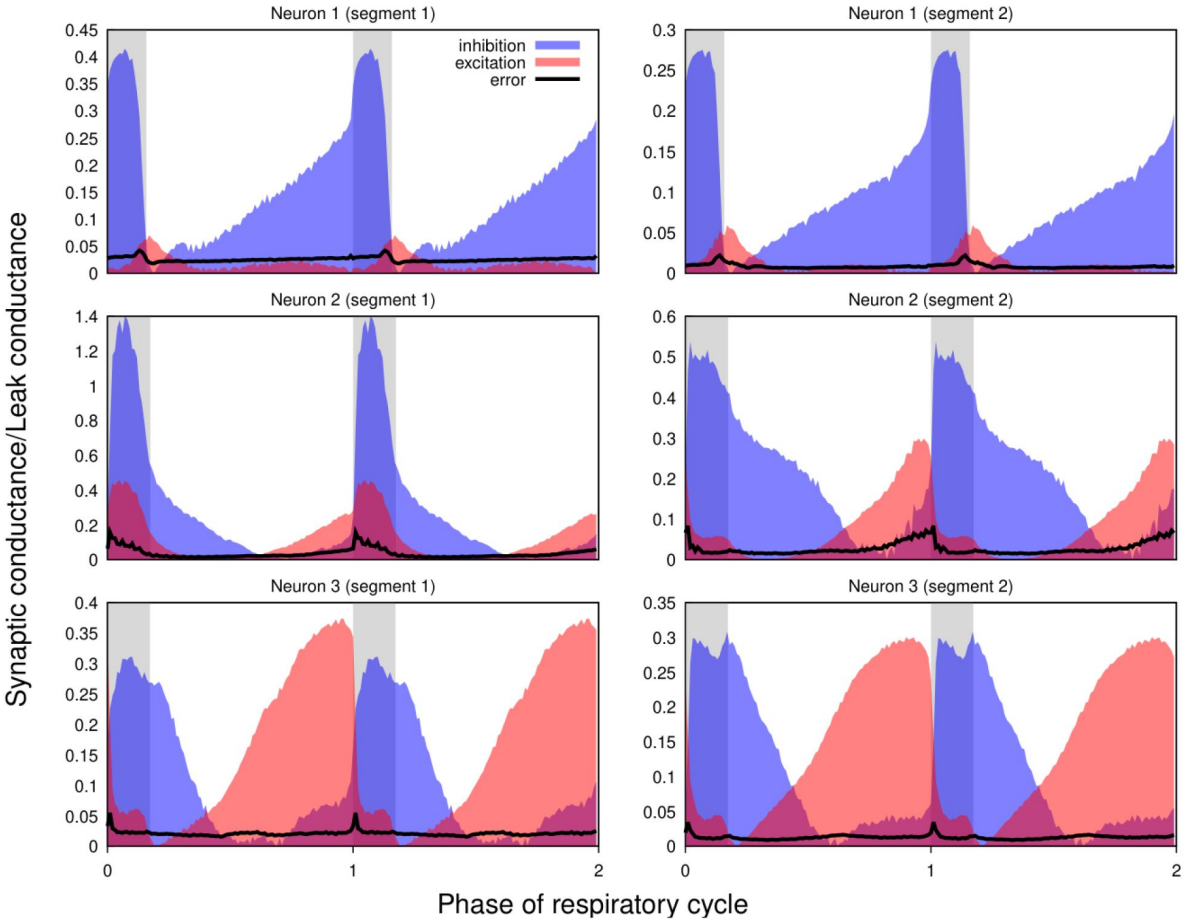

Figure 7.

Non-stationarity of the recordings does not qualitatively affect the reconstructed profiles of synaptic conductances.

Synaptic conductance profiles calculated using non-overlapping segments of the recordings (left and right) from three different neurons (post-I, top; aug-E, middle and bottom). The similarities of the conductance profiles for different segments reflect the stability of the recordings and neuronal intrinsic properties and patterns of synaptic inputs.

Figure 3), indicate that the temporal profiles of conductances obtained by our method are reliable for functional circuit reconstruction as we elaborate further below.

Discussion

In our analyses of synaptic conductance profiles in rhythmically active neurons from neuronal intracellular recordings, we propose that these profiles represent the convergent synaptic inputs from many neurons, and therefore represent the synaptic interactions of key functional populations operating in the active networks, which provides a basis for functional network reconstruction. Accordingly, a main objective of this study was to establish the utility and reliability of our technique, based on theoretical analyses and experimental validation, for extracting and separating profiles of inhibitory and excitatory conductances at high temporal resolution from intracellular recording data. We demonstrate the efficiency and robustness of our technique by applying our analyses to infer synaptic inputs to rhythmically active respiratory neurons comprising key microcircuits within the medullary preBötC and BötC regions of the brainstem respiratory CPG, which provided a diversity of neuronal electrophysiological phenotypes in various rhythmic microcircuits to test the performance of our technique. Our approach extends previously proposed methods for extracting dynamic patterns of synaptic conductances in post-synaptic neurons in various other neural circuits (Borg-Graham *et al*., 1998; Anderson *et al*., 2000; Shu *et al*., 2003; Berg *et al*., 2007; Endo & Kiehn, 2008; Wright & Calabrese, 2011), by providing higher temporal resolution with nearly continuous readouts of inhibitory and excitatory synaptic conductances, in our illustration throughout the respiratory cycle for different respiratory interneuron types. We have obtained previously unavailable synaptic conductance profiles for the different neuron populations, and illustrate how this analysis can be used to infer functional interactions and circuit configurations of interneuron populations, which demonstrates the utility of our technique. Below we further address technical issues affecting the robustness of our approach, and then discuss the general applicability to rhythmically active circuits.

Estimation of reversal potentials and errors in conductance analysis

We have noted above and evaluated uncertainties concerned with synaptic reversal potentials and assumptions about stability of the cellular properties and recordings on the inferred synaptic conductance profiles, but it is important to elaborate certain points. We have used an experimental preparation and setup that provides optimal stability for sharp electrode intracellular recordings. We used strict criteria for assessing and accepting the quality and stability of the recordings. For the most part, our analysis results for a given neuron that meets our criteria were reproducible for different recording epochs and conditions. We also generated continuous error estimates for each example shown and confirmed the statistical significance of conductance values. Regarding stationarity, our results suggest that any differences between the inferred conductance profiles for different recording epochs and conditions in most cases were comparable to those between recordings obtained by current- and voltage-clamp protocols.

Most neurons that we have analyzed receive inhibition only during certain parts of respiratory cycle regardless of whether they are inspiratory or expiratory neuron types. This allowed retrieving their reversal potentials for inhibition using the approach described in Materials and methods. Interestingly, the inhibitory synaptic reversal potentials retrieved turned out to vary significantly among cells between -62 mv and -116 mV. The reversal potential estimates were in good correspondence with actual reversals of inhibitory events when a cell was hyperpolarized below the reversal potential. Therefore, regarding the analysis, the results were reliable. Nevertheless, on average, reversal potentials were much more negative than what would have been expected. It is well known that in intracellular recordings, the length constant of the neuron

and the distance of the microelectrode from the synaptic inputs determine the measured reversal potential (Calvin, 1969; Spruston *et al*., 1993; Wehr & Zador, 2003). For the precise extraction of inhibitory and excitatory conductances from the total conductance, reversal potential values may be critical. The variability of the inhibitory reversal potential emphasizes the need to determine the reversal potential for each neuron separately. Otherwise, a wrong inhibitory reversible potential value used for the reconstruction may lead to incorrect conductance profiles. For example, a large positive bias in the inhibitory reversal potential will have the effect that a part of the inhibitory conductance may be mislabeled as excitatory conductance and therefore show a pattern of concurrent inhibition and excitation. Our method for the estimation of inhibitory reversible potential appeared very reliable when compared to the experimental estimates of the inhibitory reversal potential and essentially excluded the occurrence of this excitatory conductance artifact.

The absolute values of inhibitory and excitatory conductance calculated by the analysis are contaminated with an error depending on the length constant of the neuron and the distance of the microelectrode from the synaptic inputs (Calvin, 1969; Wehr & Zador, 2003). Importantly, Wehr and Zador (2003) show that the estimate of timing of synaptic conductances is reliable and not influenced by the length constant of the neuron. Therefore, the conductance profiles extracted with our analysis are qualitatively reliable and the overall time course of inhibitory and excitatory conductances reflect the overall inhibitory and excitatory inputs to the different electrophysiological classes of active neurons analyzed.

Applicability to any rhythmically active network

Our method for extracting and separating phasic patterns of inhibitory and excitatory synaptic conductances from single neuronal intracellular recordings is broadly applicable to rhythmic circuits which are ubiquitous in nervous systems. Our approach involves phase-based analysis, where the network activity cycle is divided into activity phases to capture dynamic changes of synaptic input conductances throughout the activity cycle. This approach is relevant for any circuits with repetitive activity cycles, such as rhythmic CPG motor networks (e.g., (Calabrese & Marder, 2024)) and circuits generating cortical rhythms (Yuste *et al*., 2005). The method is based on the general mathematical framework presented, involving current balance equations and linear regression to separate excitatory and inhibitory conductances, and therefore is applicable to different rhythmic neuron types and circuits and is suitable for diverse experimental setups. By providing high-resolution temporal profiles of synaptic inputs and outputs (below, based on neuronal spiking patterns), this method enables researchers to infer the functional connectivity and dynamic interactions within any rhythmically active network.

Applying this method, as we have illustrated for respiratory circuits, to other rhythmic networks such as locomotor or cortical circuits including sensory processing networks, follows a similar process for extracting neuronal excitatory and inhibitory inputs during different oscillatory phases of endogenous or sensory-driven periodic activity. This allows for the inference of functional synaptic input connections for any targeted neuron populations based on the timing and strength of the extracted synaptic inputs. In this context, functional populations are defined as groups of neurons with similar firing patterns with respect to the cycle phase. If the synaptic conductance profile of a recorded neuron contains a component that mirrors the firing pattern of a specific population, it can be inferred that there is a functional connection from that population to the recorded neuron. Similarly, in sensory processing networks, it can reveal how sensory inputs are synaptically integrated in neurons by examining synaptic conductance patterns in response, for example, to repetitive stimuli.

The approach that we have described is versatile since it is compatible with various recording protocols, such as current-clamp and voltage-clamp and different modes of intracellular recording (sharp electrode or whole-cell patch clamp). We note that our approach to defining functional connectivity does not provide information on locations of the sources of the synaptic inputs,

although we can infer spiking patterns of the source neurons from the temporal features of the synaptic conductance profiles. These profiles represent the total synaptic inputs that can arise from many neurons possibly with short and long-range axonal projections to a given neuron. The capability of our approach to readout the total synaptic conductance and separate the excitatory and inhibitory components from all sources at high temporal resolution is a strength of our approach. These inferred neuronal population connections from the electrophysiological analyses provided by our technique can be further mapped and corroborated with other functional and anatomical approaches.

In summary, the versatility of our technique lies in its foundation on basic electrophysiological principles and adaptability to different rhythmic activities making it a powerful tool for investigating a wide range of rhythmically active neuronal networks and potentially offering insights into their functional organization and dynamic operations.

Materials and methods

Animal procedures

All animal procedures were approved by the Animal Care and Use Committee of the National Institute of Neurological Disorders and Stroke (Animal Study Proposal #1154-21).

In situ perfused rat brain-stem spinal cord preparation

Experiments were performed using the *in situ* arterially perfused brainstem-spinal cord preparations from mature (3–4 weeks old) rats (Paton, 1996; Paton *et al*., 2022) following experimental procedures described in detail in Smith *et al*. 2007 and modified as described below to provide optimal conditions for intracellular recording. Briefly, preheparinzed (1,000 units, given intraperitoneally) rats (Sprague-Dawley, 45-70g; male) were anaesthetized deeply with 5% isoflurane and the portion of the body caudal to the diaphragm was removed. The head and thorax were immersed in ice-chilled carbogenated Ringer solution and the brain was decerebrated at a precollicular level. The descending aorta, phrenic nerve, central vagus and hypoglossal nerves were surgically isolated. The dorsal brainstem was exposed by craniotomy and cerebellectomy. To achieve the mechanical stability necessary for intracellular recordings, the great veins and heart were removed. The preparation was transferred to a recording chamber and the descending aorta cannulated with a double lumen catheter for perfusion and recording of perfusion pressure with a pressure transducer. A hydraulic damping Windkessel chamber was used in the perfusion circuit immediately downstream from the output of the roller pump (Watson-Marlow, Wilmington, MA) to eliminate peristaltic flow pulsations that affect stability of the sharp electrode intracellular recordings.

Solutions and pharmacological agents

The perfusate contained the following in distilled water: magnesium sulphate (MgSO4 -1.25 mM), potassium phosphate (KH_2PO_4 - 1.25 mM), potassium chloride (KCl - 5.0 mM), sodium bicarbonate ($NaHCO_3$ - 25 mM), sodium chloride (NaCl -125 mM), calcium chloride ($CaCl_2$ - 2.5 mM), dextrose (10 mM) and polyethylene glycol (0.1785 mM). Vecuronium bromide was added to the perfusate to block neuromuscular transmission (4 µg/ml; SUN pharmaceutical industries, Bryan, USA). The perfusate was gassed with 95%O2-5%CO2 and maintained at 31°C. Vasopressin (200–400 pM as required; APP pharmaceuticals, East Schaumburg, USA) was added to the perfusate to raise and maintain perfusion pressure at 70–80 mmHg. Unless stated, all chemicals were from Sigma.

Electrophysiological recordings and neuron labeling

Efferent activity of the phrenic (PN) and central vagus (VN) nerves were recorded simultaneously with glass suction electrodes and their activities were amplified, filtered (0.3–6.0 KHz), rectified and integrated (50 ms time constant). Sharp microelectrode somatic intracellular recordings were made in the preBötC and BötC regions. The brainstem was mapped by recording population activity of neurons in the medulla oblongata with an extracellular electrode (5–10 MOhm) prior to intracellular recording. The position of the electrode was monitored by software that kept track of the micromanipulator mechanical coordinates. Once the region of the preBötC or BötC was identified by rhythmic inspiratory/expiratory population activity, coordinates were saved and in some cases the brainstem surface was marked with pontamine sky blue dye. Intracellular recordings were made with fine tipped glass microelectrodes (45 to 70 MOhm) pulled from borosilicate glass capillaries. The microelectrodes for intracellular recording were driven into the recording site by a combination DC motor driven micromanipulator with an integrated piezotranslator (PM10-1, Marzhauser Wetzlar, Germany), allowing high stepping speeds for cell penetration. A dual current clamp-voltage clamp amplifier (SEC-05X, NPI, Tamm, Germany) was used to amplify the signals in bridge and discontinuous current clamp (DCC) recording modes. Discontinuous single electrode voltage clamp (SEVC) recordings were obtained by exploiting the high switching frequencies and electrode capacity compensation of the SEC-05X system, allowing high fidelity SEVC recordings with the high resistance sharp microelectrodes used. The microelectrodes were filled with a solution of 2 M potassium acetate (KAc) and 0.1 M potassium chloride (KCl) and 4% neurobiotin. During recordings some neurons were labeled by ionophoresis of neurobiotin into the cell. All recordings were digitized via a CED 1401-plus multi-channel interface and acquired (6–12 kHz digitization rates) using CED Spike 2 software.

Histological analysis

Transected brain stem was fixed in 4% buffered (0.1 M phosphate buffer) paraformaldehyde for 24 h at 4°C, cryoprotected at 4°C in 30% sucrose, and subsequently coronally sectioned (30 µm thick) on a freezing microtome. All the floating sections were preincubated for 1 h with 10% donkey serum in PBS and subsequently incubated for 48-72h at room temperature with primary antibodies: Rabbit anti-Glycine antibody (1:5000; Immunosolution), rabbit anti-GABA antibody (1:1000; Millipore-Sigma), and goat anti-ChAT antibody (1:500; Chemicon). Labeling for neuronal ChAT expression was used to label motoneurons of nucleus ambiguous to verify the region where the neurons were recorded and to confirm that the recordings were obtained from non-motoneurons. Floating sections were incubated for 2 h at room temperature with a mixture of donkey anti-rabbit IgG conjugated with Cy5 and donkey anti-goat IgG conjugated with Cy3 (1:500; Jackson ImmunoResearch). For fluorescence labeling of neurons filled with neurobiotin during electrophysiological recording, slices were incubated with Alexa Fluor 488-Avidin D (1:500, Invitrogen). Tissue was mounted on slides and covered with antifading medium.

Confocal images were obtained with a laser-scanning microscope (LSM 510 Meta, Zeiss). Alexa Fluor 488, Cy3, and Texas Red or Cy5 were detected at 488, 543, and 633 nm emission wavelengths, respectively. Images were acquired and processed with a Zeiss Zen software and presented as single optical sections selected from serial optical sections (Z-stacks).

Reconstruction of synaptic inputs from intracellular recordings

Preprocessing

Inhibitory and excitatory synaptic inputs to respiratory neurons were reconstructed from intracellular recordings using a general approach similar to that described by Berg *et al*. (2007) and others (Borg-Graham *et al*., 1998; Anderson *et al*., 2000; Shu *et al*., 2003; Endo & Kiehn, 2008).

During intracellular recordings for conductance measurement and subsequent decomposition of inhibitory and excitatory inputs, depolarizing and hyperpolarizing current was injected into the cell in a stepwise manner (**Figure 1A**). The period of time from the onset of the phrenic burst to the beginning of the next phrenic burst was used as reference cycle. The beginning of a phrenic burst was determined as 10% of phrenic amplitude in the rectified and low pass filtered (time constant = 0.05s) extracellular recording. We only analyzed recordings from respiratory neurons that fulfilled the following criteria: (1) The coefficient of variation of the respiratory cycle period was <10%; (2) At least three steps of current injections were made during intracellular recording that were kept constant for at least 5 respiratory cycles each. Neurons with obvious recording instability such as significant changes in membrane leakage current with a baseline membrane potential drift were not analyzed. The intracellularly recorded membrane potential $V_m(t)$ was sampled down from 12.5 kHz to 100 Hz. To eliminate spikes without affecting slow membrane potential fluctuations the voltage trace $V_m(t)$ was processed using median filtration.

Error estimation

After performing linear regression (2) for each phase bin we have standard errors $\delta R(\phi)$ and $\delta V_0(\phi)$ of the total resistance $R(\phi)$ and the resting potential $V_0(\phi)$ respectively which are defined by voltage fluctuations and by the number of respiratory cycles in the epoch used for reconstruction. Based on this we can approximately calculate the standard error for the total conductance $\delta G(\phi) = \delta R(\phi)/R^2(\phi)$, which can be used as an overestimate for the errors of both excitatory and inhibitory conductances since the total conductance is a sum of the two. Calculation of the dynamic components involves subtraction of the minimal values of the calculated synaptic conductances. Therefore, the dynamic components' standard errors can be estimated as $\delta\Delta G_{i,e}(\varphi) = \sqrt{\delta G(\varphi)^2 + \delta G(\varphi_m)^2}$, where ϕ_m is the phase where the corresponding conductance (excitatory or inhibitory) attains its minimum.

Statistical significance

Considering the relatively large sample sizes (for each cell analyzed we had 50-200 respiratory cycles long recordings), we used a one-tailed z-test to confirm statistical significance of the reconstructed synaptic inputs by testing a null hypothesis that the dynamical component of the synaptic conductance is zero (no different from its minimal value). Specifically, at each phase of the respiratory cycle ϕ for the dynamic components of inhibitory and excitatory conductances we calculated their z-scores $Z_{i,e}(\phi) = \Delta G_{i,e}(\phi)/\delta\Delta G_{i,e}(\phi)$, and corresponding p-values. We used p-value < 0.05 criterion to accept the alternative hypothesis that the calculated dynamic component of the synaptic conductance at a particular phase is statistically significantly greater than zero. In the latter case, we concluded that the recorded cell received the corresponding type of synaptic input (excitatory or inhibitory) during the corresponding part of the respiratory cycle (inspiration, post-inspiration, or late-expiration/pre-inspiration).

Acknowledgements

This study was supported by NIH grants R01 NS057815, R01 NS069220, R01 AT008632, Alexander von Humboldt Foundation, and the Intramural Research Program of the NIH, NINDS.

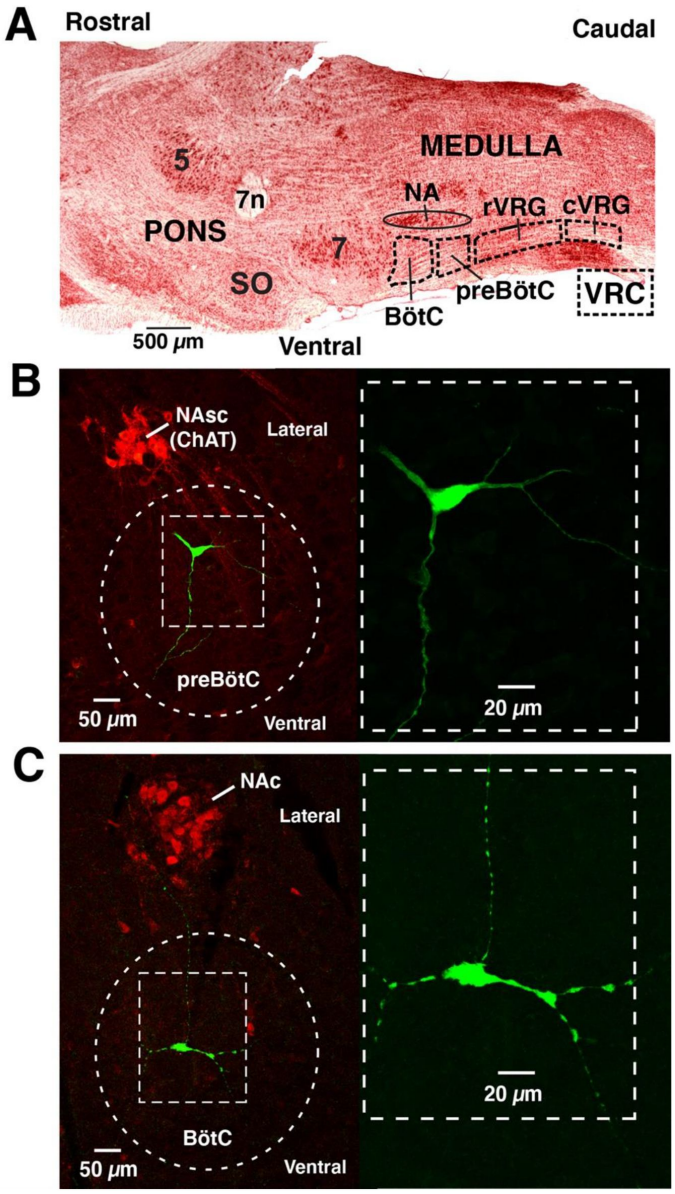

Supplemental Figure 1.

Respiratory regions of the brainstem ventrolateral medulla and intracellular recording sites.

A. Parasagittal view (neutral red stain) of the lateral medulla indicating regions of the ventral respiratory column (VRC) and locations of the preBötC and BötC regions of the VRC in the ventrolateral medulla, ventral to nucleus ambiguus (NA) that were targeted for intracellular recordings. Abbreviations: rVRG and cVRG, rostral and caudal ventral respiratory groups which also contain neurons of the respiratory CPG; 5 and 7, trigeminal and facial motor nuclei; 7n, facial nerve; SO, superior olivary nuclei. **B**. Example of histological reconstruction (confocal fluorescence images) of recorded inspiratory neuron (ramp-I) in the preBötC region ventral to motoneurons of NAsc (semi-compact division) labeled by immunostaining (red) for choline acetyltransferase (ChAT). The locations of rhythmic neurons used for our analyses were routinely verified by filling the cells with neurobiotin by iontophoresis at the end of recording and fluorescently stained (see Methods), and in some cases further processed for immuno-identification of neurotransmitter phenotype (see **Supplemental Figure 2**). The immunostaining for ChAT was used as a landmark for regional recording locations, and also to verify that recordings were obtained from interneurons and not motoneurons. A higher magnification image of neuronal morphology with background removed is shown in the dashed box at right. **C**. Example of histological reconstruction (confocal images) of a recorded expiratory neuron (aug-E) and fluorescently stained in the BötC region ventral to motoneurons of NAc (compact division) labeled by immunostaining (red) for ChAT. Higher magnification image of labeled neuron (background removed) is shown at right.

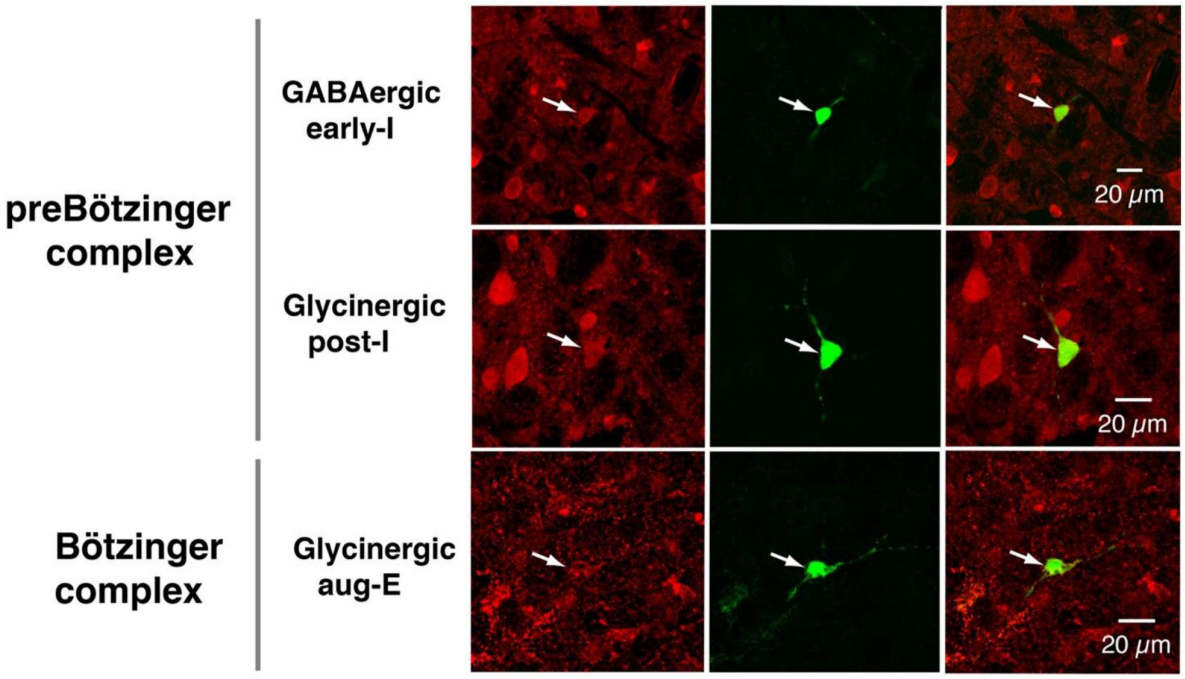

Supplemental Figure 2.

Identification of glycinergic or GABAergic inhibitory neurons.

Examples from separate experiments of neurons filled with neurobiotin during the somatic intracellular recordings, and subsequent immunohistochemistry with antibodies for glycine or GABA (red fluorescence), and Alexa Fluor 488-Avidin D conjugate to label neurobiotin. Images shown for the labeled respiratory neuron types in the ventrolateral medullary regions indicated are fluorescence single-plane confocal images for the glycine or GABA antibody labeling (left panels), neurobiotin labeling (middle), and superposition images showing double labeling (right). The single imaging planes shown were chosen to optimize visualization of co-labeling of the somata of the recorded neuron in each case.

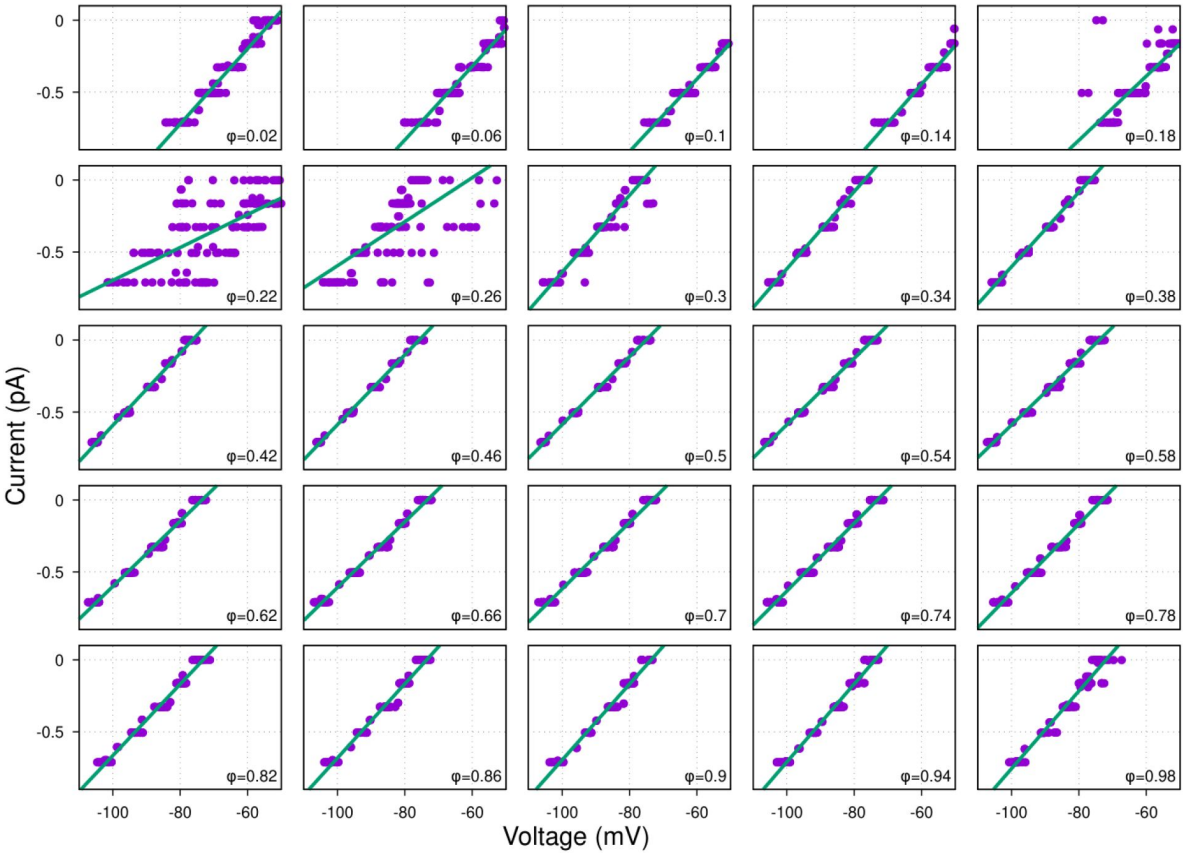

Supplemental Figure 3.

Linear regressions of the injected current vs. membrane voltage for different phases of the respiratory cycle.

Shown are the injected current (y-axis) vs. membrane voltage (x-axis) relations for 25 different phases of the respiratory cycle from a current-clamp recording from a ramp-I preBötC neuron. The phase value is indicated in the bottom right corner of each plot. This figure illustrates that the phase-specific current-voltage dependencies are almost perfectly linear in a wide range of voltage values. The exception is the interval of phase values near the transition from inspiration to expiration (0.2-0.25 for this particular recording) which reflects some cycle-cycle variability of the inspiratory phase durations. Less perfect linear fits near the transitions between respiratory phases manifest as bumps in the error estimates shown by black lines in **Figures 1D**, **3**, **5**, **6**, **7**.

References

Anderson JS, Carandini M, Ferster D. (2000) **Orientation tuning of input conductance, excitation, and inhibition in cat primary visual cortex** *J Neurophysiol* **84**:909–926

Ausborn J, Koizumi H, Barnett WH, John TT, Zhang R, Molkov YI, Smith JC, Rybak IA (2018) **Organization of the core respiratory network: Insights from optogenetic and modeling studies** *PLoS Comput Biol* **14**

Berg RW, Alaburda A, Hounsgaard J. (2007) **Balanced inhibition and excitation drive spike activity in spinal half-centers** *Science* **315**:390–393

Bianchi AL, Denavitsaubie M, Champagnat J. (1995) **Central Control of Breathing in Mammals - Neuronal Circuitry, Membrane-Properties, and Neurotransmitters** *Physiological Reviews* **75**:1–45

Borg-Graham LJ, Monier C, Fregnac Y. (1998) **Visual input evokes transient and strong shunting inhibition in visual cortical neurons** *Nature* **393**:369–373

Buzsáki G. (2006) **Rhythms of the brain** Oxford ; New York: Oxford University Press

Calabrese RL, Marder E. (2024) **Degenerate Neuronal and Circuit Mechanisms Important for Generating Rhythmic Motor Patterns** *Physiological Reviews* in press

Calvin WH (1969) **Dendritic synapses and reversal potentials: theoretical implications of the view from the soma** *Exp Neurol* **24**:248–264

Cohen MI (1979) **Neurogenesis of respiratory rhythm in the mammal** *Physiol Rev* **59**:1105–1173

Endo T, Kiehn O. (2008) **Asymmetric operation of the locomotor central pattern generator in the neonatal mouse spinal cord** *J Neurophysiol* **100**:3043–3054

Ezure K, Tanaka I, Kondo M. (2003) **Glycine is used as a transmitter by decrementing expiratory neurons of the ventrolateral medulla in the rat** *The Journal of neuroscience : the official journal of the Society for Neuroscience* **23**:8941–8948

Feldman JL, Smith JC, Dempsey JA, Pack AI (1995) **Neural Control of Respiratory Pattern in Mammals: An Overview** *In Regulation of breathing* New York: M. Dekker :39–69

Lindsey BG, Rybak IA, Smith JC (2012) **Computational models and emergent properties of respiratory neural networks** *Compr Physiol* **2**:1619–1670

Molkov YI, Rubin JE, Rybak IA, Smith JC (2017) **Computational models of the neural control of breathing** *Wiley Interdiscip Rev Syst Biol Med* **9**

Paton JF (1996) **A working heart-brainstem preparation of the mouse** *J Neurosci Methods* **65**:63–68

Paton JFR *et al.* (2022) **Advancing respiratory-cardiovascular physiology with the working heart-brainstem preparation over 25 years** *J Physiol* **600**:2049–2075

Richter DW, Greger R, Windhorst U (1996) **Neural regulation of respiration: rhythmogenesis and afferent control** *In Comprehensive Human Physiology* Berlin: Springer-Verlag :2079–2095

Richter DW, Smith JC (2014) **Respiratory rhythm generation in vivo** *Physiology (Bethesda)* **29**:58–71

Richter DW, Spyer KM (2001) **Studying rhythmogenesis of breathing: comparison of in vivo and in vitro models** *Trends Neurosci* **24**:464–472

Shu Y, Hasenstaub A, McCormick DA (2003) **Turning on and off recurrent balanced cortical activity** *Nature* **423**:288–293

Smith JC, Abdala AP, Borgmann A, Rybak IA, Paton JF (2013) **Brainstem respiratory networks: building blocks and microcircuits** *Trends Neurosci* **36**:152–162

Spruston N, Jaffe DB, Williams SH, Johnston D. (1993) **Voltage- and space-clamp errors associated with the measurement of electrotonically remote synaptic events** *J Neurophysiol* **70**:781–802

Wehr M, Zador AM (2003) **Balanced inhibition underlies tuning and sharpens spike timing in auditory cortex** *Nature* **426**:442–446

Wright TM, Calabrese RL (2011) **Patterns of presynaptic activity and synaptic strength interact to produce motor output** *J Neurosci* **31**:17555–17571

Yuste R, MacLean JN, Smith J, Lansner A. (2005) **The cortex as a central pattern generator** *Nat Rev Neurosci* **6**:477–483

Editors

Reviewing Editor
John Huguenard
Stanford University School of Medicine, Stanford, United States of America

Senior Editor
John Huguenard
Stanford University School of Medicine, Stanford, United States of America

Reviewer #1 (Public review):

Summary:

The paper develops a phase method to obtain the excitatory and inhibitory afferents to certain neuron populations in the brainstem. The inferred contributions are then compared to the results of voltage clamp and current clamp experiments measuring the synaptic contributions to post-I, aug-E, and ramp-I neurons.

Strengths:

The electrophysiology part of the paper is sound and reports novel features with respect to earlier work by JC Smith et al 2012, Paton et al 2022 (and others) who have mapped circuits of the respiratory central pattern generator. Measurements on ramp-I neurons, late-I neurons, and two types of post-I neurons in Figure 2 besides measurements of synaptic inputs to these neurons in Figure 5 are to my knowledge new.

Weaknesses:

The phase method for inferring synaptic conductances fails to convince. The method rests on many layers of assumptions and the inferred connections in Figure 4 remain speculative. To be convincing, such a method ought to be tested first on a model CPG with known connectivity to assess how good it is at inferring known connections back from the analysis of spatio-temporal oscillations. For biological data, once the network connectivity has been inferred as claimed, the straightforward validation is to reconstruct the experimental oscillations (Figure 2) noting that Rybak et al (Rybak, Paton Schwaber J. Neurophysiol. 77, 1994 (1997)) have already derived models for the respiratory neurons.

The transformation from time to phase space, unlike in the Kuramoto model, is not justified here (Line 94) and is wrong. The underpinning idea that "the synaptic conductances depend on the cycle phase and not on time explicitly" is flawed because synapses have characteristic decay times and delays to response which remain fixed when the period of network oscillations increases. Synaptic properties depend on time and not on phase in the network. One major consequence relevant to the present identification of excitatory or inhibitory behaviour, is that it cannot account for change in the behaviour of inhibitory synapses - from inhibitory to excitatory action - when the inhibitory decay time becomes commensurable to the period of network oscillations (Wang & Buzsaki Journal of Neuroscience 16, 6402 (1996), van Vreeswijk et al. J. Comp. Neuroscience 1,313 (1994), Borgers and Kopell Neural Comput. 15, 2003). In addition, even small delays in the inhibitory synapse response relative to the pre-synaptic action potential also produce in-phase synchronization (Chauhan et al., Sci. Rep. 8, 11431 (2018); Borgers and Kopell, Neural Comput. 15, 509 (2003)). The present assumptions are way too simplistic because you cannot account for these commensurability effects with a single parameter like the network phase. There is therefore little confidence that this model can reliably distinguish excitatory from inhibitory synapses when their dynamic properties are not properly taken into account.

Line 82, Equation 1 makes extremely crude assumptions that the displacement current (CdV/dt) is negligible and that the ion channel currents are all negligible. Vm(t) is also not defined. The assumption that the activation/inactivation times of all ion channels are small compared to the 10-20ms decay time of synaptic currents is not true in general. Same for the displacement current. The leak conductance is typically g~0.05-0.09ms/cm^2 while C~1uF/cm^2. Therefore the ratio C/g leak is in the 10-20ms range - the same as the typical docking neurotransmitter time in synapses.

Models of brainstem CPG circuits have been known to exist for decades: JC Smith et al 2012, Paton et al 2022, Bellingham Clin. Exp. Pharm. And Physiol. 25, 847 (1998); Rubin et al., J. Neurophysiol. 101, 2146 (2009) among others. The present paper does not discuss existing knowledge on respiratory networks and gives the impression of reinventing the wheel from scratch. How will this paper add to existing knowledge?

https://doi.org/10.7554/eLife.101959.1.sa1

Reviewer #2 (Public review):

Summary:

By measuring intracellular changes in membrane voltage from a single neuron of the medulla the authors describe a method for determining the balance of excitatory and inhibitory synaptic drive onto a single neuron within this important brain region.

Strengths:

This approach could be valuable in describing the microcircuits that generate rhythms within this respiratory control centre. This method could more generally be used to enable microcircuits to be studied without the need for time-consuming anatomical tracing or other more involved electrophysiological techniques.

Weaknesses:

This approach involves assuming the reversal potential that is associated with the different permeant ions that underlie the excitation and inhibition as well as the application of Ohms law to estimate the contribution of excitation and inhibitory conductance. My first concern is that this approach relies on a linear I-V relationship between the measured voltage and the estimated reversal potential. However, open rectification is a feature of any I-V relationship generated by asymmetric distributions of ions (see the GHK current equation) and will therefore be a particular issue for the inhibition resulting from asymmetrical Cl- ion gradients across GABA-A receptors. The mixed cation conductance that underlies most synaptic excitation will also generate a non-linear I-V relationship due to the inward rectification associated with the polyamine block of AMPA receptors. Could the authors please speculate what impact these non-linearities could have on results obtained using their approach?

This approach has similarities to earlier studies undertaken in the visual cortex that estimated the excitatory and inhibitory synaptic conductance changes that contributed to membrane voltage changes during receptive field stimulation. However, these approaches also involved the recording of transmembrane current changes during visual stimulation that were undertaken in voltage-clamp at various command voltages to estimate the underlying conductance changes. Molkov et al have attempted to essentially deconvolve the underlying conductance changes without this information and I am concerned that this simply may not be possible. The current balance equation (1) cited in this study is based on the parallel conductance model developed by Hodgkin & Huxley. However, one key element of the HH equations is the inclusion of an estimate of the capacitive current generated due to the change in voltage across the membrane capacitance. I would always consider this to be the most important motivation for the development of the voltage-clamp technique in the 1930's. Indeed, without subtraction of the membrane capacitance, it is not possible to isolate the transmembrane current in the way that previous studies have done. In the current study, I feel it is important that the voltage change due to capacitive currents is taken into consideration in some way before the contribution of the underlying conductance changes are inferred.

Studies using acute slicing preparations to examine circuit effects have often been limited to the study of small microcircuits - especially feedforward and feedback interneuron circuits. It is widely accepted that any information gained from this approach will always be compromised by the absence of patterned afferent input from outside the brain region being studied. In this study, descending control from the Pons and the neocortex will not be contributing much to the synaptic drive and ascending information from respiratory muscles will also be absent completely. This may not have been such a major concern if this study was limited to demonstrating the feasibility of a methodological approach. However, this limitation does need to be considered when using an approach of this type to speculate on the prevalence of specific circuit motifs within the medulla (Figure 4). Therefore, I would argue that some discussion of this limitation should be included in this manuscript.

https://doi.org/10.7554/eLife.101959.1.sa0